

Supervised Manifold Learning-Based Polarimetric-Spatial Feature Extraction for PolSAR Image Classification

Hui Fan¹, Wei Wang^{2,*}, Sinong Quan², Xi He³, and Jie Deng²

¹College of Electronic Information and Physics, Central South University of Forestry and Technology, Changsha 410004, China

²College of Electronic Science and Technology, National University of Defense Technology, Changsha 410073, China

³College of Bangor, Central South University of Forestry Technology, Changsha 410004, China

ABSTRACT: In order to improve the classification performance of Polarimetric Synthetic Aperture Radar (PolSAR) image by synthesizing various polarimetric features, a supervised manifold learning method is proposed in this paper for PolSAR feature extraction and classification. Under the umbrella of tensor algebra, the proposed method characterizes each pixel with a feature tensor by combining the high-dimensional feature information of all the pixels within its local neighborhood. The tensor representation mode integrates the polarimetric information and spatial information, which is beneficial for alleviating the influence of speckle noise. Then, the tensor discriminative locality alignment (TDLA) method is introduced to seek the multilinear transformation from the original polarimetric-spatial feature tensor to the low-dimensional feature. The label information of training samples is utilized during feature transformation and feature mapping; therefore, the discriminability of different classes can be well preserved. Based on the extracted features in the low-dimensional space, the SVM classifier is applied to achieve the final classification result. The experiments implemented on two real PolSAR data sets verify that the proposed method can extract the features with better stability and separability, and obtain superior classification results compared to several state-of-the-art methods.

1. INTRODUCTION

Polarimetric Synthetic Aperture Radar (PolSAR) is an advanced SAR system that can obtain more comprehensive scattering information of land covers and targets by adjusting the polarization of transmitting/receiving electromagnetic waves, and it has been increasingly used in the fields of earth observation, reconnaissance, environment monitoring, disaster assessment, etc. [1]. Land use/land cover (LULC) classification, as one of the research hotspots in PolSAR image interpretation, has aroused many researchers' interest [2]. Generally, there are two main steps in PolSAR classification methods, i.e., feature extraction and classifier design, whereas the former step is more crucial and determines the performance of image classification to a large extent.

According to the polarimetric information or features that are used, PolSAR classification methods can be basically categorized into three types, i.e., the methods relying on statistical modeling [3, 4], the methods based on polarimetric decomposition [5, 6], and the methods that use a combination of multiple features (statistical features, decomposition features, texture features, etc.) [7–9]. Polarimetric target decomposition represents PolSAR data as a linear combination of several basic scattering mechanisms which possess specific physical meaning, and it has been a significant tool for polarimetric feature extraction. Based on the polarimetric decomposition features, satisfactory classification results can be achieved by using conventional classifiers, such as support vector machine (SVM) and

K-nearest neighbor (KNN). The polarimetric decomposition-based classification method has been widely used in various PolSAR applications, due to its good interpretability and low computational complexity.

With the continuous development of polarimetric target decomposition theory, various decomposition methods have been proposed, including Freeman three-component decomposition [10], Yamaguchi four-component decomposition [11], multi-component target decomposition [12], etc. However, for a single polarimetric decomposition method, the extracted feature or feature set cannot effectively distinguish different types of land covers in some scenes, and cause misclassifications. This is because different land covers may possess similar scattering mechanism, and the same class of land cover can incur different scattering mechanisms. For example, the buildings not aligned orthogonally to radar line of sight (namely oriented buildings) also cause cross-polarized scattering, which can be easily confused with vegetation. To solve the problem of scattering mechanism confusion, some new polarimetric decomposition methods [13, 14] are proposed by constructing cross-scattering components which are applicable to the building areas. However, the polarimetric features extracted by a single decomposition method still cannot meet the requirement of refined classification in complex scenarios. More and more scholars are engaged to improve the classification performance by combining the features obtained by multiple decomposition methods. However, these signatures are correlated, and the simple combination of different features introduces information redundancy, thus increasing

* Corresponding author: Wei Wang (wwang@nudt.edu.cn).

the complexity of classification processing and even causing “dimension catastrophe”. Therefore, it is vital to process multiple polarimetric features comprehensively beforehand, so that the main information in the feature space can be retained while the feature dimensionality can be reduced to a large extent.

There are two types of ways to obtain valuable low-dimensional features, namely, feature selection [15] and feature extraction. Feature selection aims to select an optimal feature subset under certain evaluation criteria while feature extraction means projecting high-dimensional features into a low-dimensional subspace so that the intrinsic and discriminative information can be well preserved. With regards to feature extraction or feature dimensionality reduction, principal component analysis (PCA) [16], linear discriminant analysis (LDA), and independent component analysis (ICA) are the most commonly used methods, which are based on linear projection. Nonlinear manifold learning methods have also been applied to feature dimensionality reduction of PolSAR data. For example, Tu et al. used the Laplacian eigenmap (LE) method to project 42-dimensional feature vector into a low-dimensional feature vector [17]. In addition, tools such as local linear embedding (LLE) [18] and isometric feature mapping (Isomap) [19] have been applied to PolSAR feature extraction and image classification. Those manifold-related methods firstly construct a neighborhood graph between pixels, and the manifold structure representing the relationship among PolSAR data is preserved during feature extraction [20]. However, these methods have high computational burden and are sensitive to outliers and noise. In addition, the methods mentioned above are unsupervised, which means that the discriminative information of the samples is not exploited in feature extraction procedure. To take the advantage of the label information, Shi et al. applied the supervised graph embedding (SGE) method and obtained low-dimensional features with better discriminability [21].

However, these methods deal with each pixel independently, and the spatial relationship with neighboring pixels is neglected. In fact, the spatial information can help to alleviate the influence of speckle noise in PolSAR data and improve the classification performance. Therefore, it is necessary to make full use of the feature information of multiple pixels within a local neighborhood, so as to improve the accuracy and reliability of the extracted features. In recent years, tensor algebra-based methods have attracted much attention, since they provide an effective technical means for high-order data processing and are widely applied in computer vision, hyperspectral image analysis, LiDAR data processing, etc. [22–24]. Under the umbrella of multilinear algebra and tensor decomposition, many tensor subspace learning methods have been developed [25, 26], which lay the basis of feature extraction in high-dimensional space. These methods seek an optimal linear transformation, which can preserve the local properties of the original data distribution in the feature subspace [27]. Tao et al. for the first time utilize tensor-based technique for PolSAR data processing [28], in which tensor decomposition and ICA are combined. However, the class information of the available samples is not used in this method. Recently, tensor local discriminant embed-

ding (TLDE) and other tensorial feature extraction techniques have been proposed for PolSAR classification [29]. In these methods, the feature tensor for each pixel is usually constructed based on the patch centered on the pixel. The fixed structure of the neighborhood may affect the performance of PolSAR classification, especially in some complex areas.

Motivated by the above works, a supervised manifold learning-based method is proposed in this paper for PolSAR feature extraction and classification. At first, based on the acquisition of typical decomposition features of PolSAR data, the proposed method characterizes each pixel with a feature tensor by combining the feature vectors within a local neighborhood which has flexible shape. Then, the tensor discriminative locality alignment (TDLA) method [27] is introduced to seek the multilinear transformation from the original feature space to the feature subspace. A generalized framework of tensor manifold learning is presented which can maintain the manifold structure and the most prominent features of pixels. Based on the extracted features, the SVM classifier is employed to achieve the final classification result. The tensor characterization in this method preserves the polarimetric-spatial information and helps to suppress the effect of speckle noise. In addition, the label information of training samples is utilized during manifold learning and feature extraction; therefore, the discriminability of different classes can be well preserved.

The remainder of this paper is organized as follows. Section 2 introduces the tensor fundamentals. Section 3 describes the proposed method in details. The experimental results on two real PolSAR data sets are given in Section 4. Section 5 concludes this paper.

2. TENSOR ALGEBRA

Tensor algebra is an extension of conventional linear algebra in high dimensional spaces. Given a tensor $\mathbf{X} \in \mathbf{R}^{L_1 \times L_2 \times \dots \times L_M}$, in which \mathbf{M} is the order, then L_i ($1 \leq i \leq M$) is the size of i th order (aka mode or way) of \mathbf{X} , and an element of \mathbf{X} is expressed as $\mathbf{X}_{l_1, l_2, \dots, l_M}$, where $1 \leq l_i \leq L_i$. Scalars, vectors, and matrices are all special forms of tensor, whose orders are 0, 1, and 2, respectively. Definitions of common multidimensional linear algebraic operations of tensors are as follows [30]:

(1) Tensor Inner Product. The inner product of two tensors \mathbf{X} , \mathbf{Y} , with dimensions are completely identical which is defined as:

$$\langle \mathbf{X}, \mathbf{Y} \rangle = \sum_{l_1=1}^{L_1} \sum_{l_2=1}^{L_2} \dots \sum_{l_M=1}^{L_M} \mathbf{X}_{l_1, l_2, \dots, l_M} \mathbf{Y}_{l_1, l_2, \dots, l_M}. \quad (1)$$

Then the Frobenius norm of a tensor is defined as $\|\mathbf{X}\| = \sqrt{\langle \mathbf{X}, \mathbf{X} \rangle}$, and the distance between two tensors is given by $D(\mathbf{X}, \mathbf{Y}) = \|\mathbf{X} - \mathbf{Y}\|$.

(2) The Mode- d Unfolding. An arbitrary order of $\mathbf{X} \in \mathbf{R}^{L_1 \times L_2 \times \dots \times L_d \times \dots \times L_M}$ tensor can be unfolded into a matrix. The matrix obtained by unfolding the mode- d is denoted as $\text{Mat}_d(\mathbf{X}) \in \mathbf{R}^{L_d \times \bar{L}_d}$, where $\bar{L}_d = \prod_{i=1, i \neq d}^M L_i$. The mode- d unfolding of a tensor is arranging L_d mode- d fibres (vectors

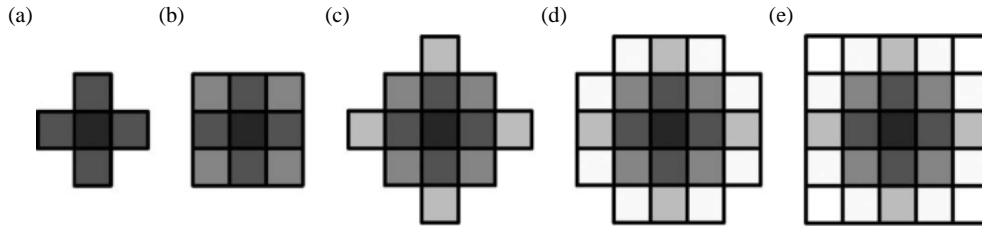


FIGURE 1. The structures of different neighborhoods. (a) 4-nearest neighborhood; (b) 8-nearest neighborhood; (c) 12-nearest neighborhood; (d) 20-nearest neighborhood; (e) 24-nearest neighborhood.

obtained along the d -dimension of the tensor \mathbf{X} into a matrix, where the elements are the same as those in the original tensor.

(3) The Mode- d Product. The mode- d product of a tensor $\mathbf{X} \in \mathbf{R}^{L_1 \times L_2 \times \dots \times L_d \times \dots \times L_M}$ and a matrix $\mathbf{U} \in \mathbf{R}^{L'_d \times L_d}$ is a tensor denoted as $(\mathbf{X} \times_d \mathbf{U}) \in \mathbf{R}^{L_1 \times L_2 \times \dots \times L_{d-1} \times L'_d \times L_{d+1} \times \dots \times L_M}$, obtained by:

$$\begin{aligned} & (\mathbf{X} \times_d \mathbf{U})_{l_1, l_2, \dots, l_{d-1}, l'_d, l_{d+1}, \dots, l_M} \\ &= \sum_{l_d=1}^{L_d} \left(\mathbf{X}_{l_1, l_2, \dots, l_d, \dots, l_M} \mathbf{U}'_{l'_d, l_d} \right). \end{aligned} \quad (2)$$

(4) In addition, the mode- d product of a tensor \mathbf{X} and a matrix \mathbf{U} satisfies the following equation:

$$\mathbf{Y} = \mathbf{X} \times_d \mathbf{U} \Leftrightarrow \text{Mat}_d(\mathbf{Y}) = \mathbf{U} \times \text{Mat}_d(\mathbf{X}). \quad (3)$$

(5) Tensor contraction. Given tensors $\mathbf{X} \in$

$\mathbf{R}^{L_1 \times L_2 \times \dots \times L_M \times L'_1 \times L'_2 \times \dots \times L'_{M_1}}$ and $\mathbf{Y} \in \mathbf{R}^{L_1 \times L_2 \times \dots \times L_M \times L''_1 \times L''_2 \times \dots \times L''_{M_2}}$, the contraction of them is defined as:

$$\begin{aligned} & [\mathbf{X} \otimes \mathbf{Y}; (1 : M)(1 : M)] = \sum_{l_1=1}^{L_1} \sum_{l_2=1}^{L_2} \dots \sum_{l_M=1}^{L_M} \\ & \mathbf{X}_{l_1, l_2, \dots, l_M, l'_1, l'_2, \dots, l'_{M_1}} \mathbf{Y}_{l_1, l_2, \dots, l_M, l''_1, l''_2, \dots, l''_{M_2}}. \end{aligned} \quad (4)$$

The condition of the contraction is that the sizes of tensor \mathbf{X} and \mathbf{Y} are the same at one or multiple modes, which means that the number of elements in that dimension is the same. The resulting tensor obtained from the above contraction equation is of mode $M_1 + M_2$. For tensors that are of same size $\mathbf{X}, \mathbf{Y} \in \mathbf{R}^{L_1 \times L_2 \times \dots \times L_M}$, the full contraction of them from mode 1 to mode M is equivalent to taking their inner product.

3. METHODOLOGY

3.1. Tensor Representation of PolSAR Data

PolSAR data is usually expressed by the covariance matrix \mathbf{C} or the coherence matrix \mathbf{T} after multilook processing on the basis of the scattering matrix \mathbf{S} . It is difficult to obtain satisfactory classification results if the elements in the matrix are directly fed into a typical classifier for classification process. Researchers have further processed these matrices and proposed many polarimetric decomposition methods to obtain features

representing different scattering types, as described in the introduction. Using the classical polarimetric decomposition methods, based on the covariance matrix \mathbf{C} , different decomposition features can be calculated. Table 1 lists 48 polarimetric features containing 9 independent elements of the covariance matrix.

On the basis of polarimetric feature extraction, the information of each pixel can be represented using a 48-dimensional feature vector. Traditional feature dimensionality reduction methods process these feature vectors separately to obtain low-dimensional feature vectors. However, this processing does not take advantage of the spatial structure information inherent in the image.

To solve this problem, this paper uses tensor algebra to combine the polarimetric information of pixels with spatial information. Specifically, for any pixel, its feature vector can be represented as $x \in \mathbf{R}^L$ ($L = 48$), and by combining x with the feature vectors x_i ($i = 1, 2, \dots, k$) at all positions in the neighboring space, the second-order feature tensor representing the information of that pixel can be obtained, denoted as:

$$\mathbf{X} = [x, x_1, x_2, \dots, x_k] \in \mathbf{R}^{L \times (k+1)}. \quad (5)$$

Among them, k represents the number of neighboring pixels. Figure 1 shows the structures of different neighborhoods, on which different feature tensors of various sizes can be constructed.

Figure 2 shows the illustration of construction of feature tensor. Firstly, different polarimetric features are obtained based on polarimetric SAR data. Then, for each pixel, the corresponding feature tensor is constructed according to the selected neighborhood structure. In this figure, an 8-neighborhood structure is selected, so the information of each pixel is represented using the feature tensor of $\mathbf{X} \in \mathbf{R}^{L_1 \times L_2}$ ($L_1 = 48, L_2 = 9$).

3.2. Supervised Manifold Learning-Based Feature Extraction

A great deal of redundant information is contained in feature tensor. In order to extract main polarimetric information for subsequent classification, the TDLA algorithm [27] is introduced to obtain a multilinear transformation matrix from the original polarimetric feature tensor $\mathbf{X} \in \mathbf{R}^{L_1 \times L_2}$ to the reduced feature tensor. Given the reduced feature tensor $\mathbf{X}^* \in \mathbf{R}^{d_1 \times d_2}$, where $d_1 \leq L_1$ and $d_2 \leq L_2$. The goal of TDLA algorithm is to seek a multilinear transformation matrix $\mathbf{U}_i \in \mathbf{R}^{L_i \times d_i}$ ($i = 1, 2$), which satisfies the correlation below:

$$\mathbf{X}^* = \mathbf{X} \times_1 \mathbf{U}_1^T \times_2 \mathbf{U}_2^T. \quad (6)$$

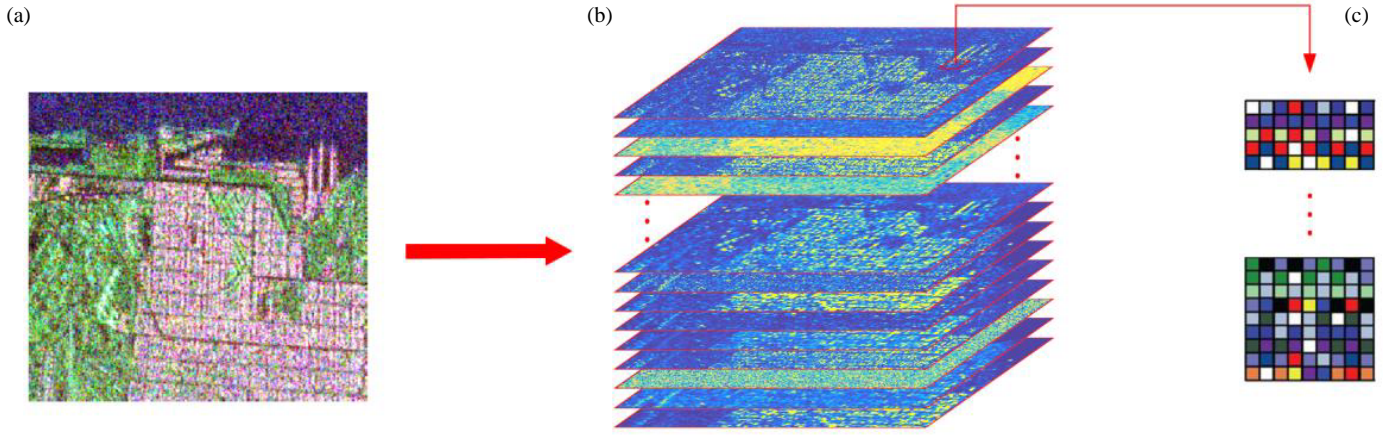


FIGURE 2. Illustration of feature tensor construction. (a) Original PolSAR data; (b) Classic polarimetric features; (c) Feature tensor.

TABLE 1. Polarimetric features obtained using different methods.

Method	Polarimetric feature		
	C11	C22	C33
Elements of Covariance matrix (9)	C12_modulus	C12_phase	C13_phase
	C13_modulus	C23_modulus	C23_phase
	Cloude [31] (3)	Cloude_C11	Cloude_C22
Freeman [10] (3)	Freeman_Odd	Freeman_Dbl	Freeman_Vol
VanZyl [32] (3)	VanZy_Odd	VanZy_Dbl	VanZy_Vol
Krogager [33] (3)	Krogager_Ks	Krogager_Kd	Krogager_Kh
	Yamaguchi [11] (4)	Yamaguchi_Dbl	Yamaguchi_Vol
H/A/Alpha [5] (6)	Yamaguchi_Odd		
	Yamaguchi_Hlx		
Huynen [34] (3)	Entropy	Alpha	Anisotropy
	Lambda1	Lambda2	Lambda3
An&Yang [35] (4)	Huynen_C11	Huynen_C22	Huynen_C33
	An_Yang_Odd	An_Yang_Dbl	An_Yang_Vol
Zhang [12] (5)	An_Yang_Hlx		
	Zhang_Odd	Zhang_Dbl	Zhang_Vol
Xiang [13] (5)	Zhang_Hlx	Zhang_Wire	
	Xiang_Odd	Xiang_Dbl	Xiang_Vol
	Xiang_Hlx	Xiang_Cros	

The input data of the TDLA algorithm is a set of training samples, including feature tensors \mathbf{X}_i ($i = 1, 2, \dots, N$) and corresponding class labels $y_i \in [1, 2, \dots, C]$ of the samples, in which N is the number of samples, and C is the number of classes. For each training sample \mathbf{X}_i , the rest $N - 1$ samples are divided into two groups: the same class samples and the different class samples. Within the two groups, samples are sequenced in terms of the tensor distance between the corresponding sample and tensor \mathbf{X}_i . Then the first n_1 samples with shorter distance in “same class” and the first n_2 samples in “different classes” are selected to combine with \mathbf{X}_i itself, thus building local alignment of \mathbf{X}_i :

$$\text{Patch}(\mathbf{X}_i) = \{\mathbf{X}_i, \mathbf{S}_{i(1)}, \dots, \mathbf{S}_{i(n_1)}, \mathbf{D}_{i(1)}, \dots, \mathbf{D}_{i(n_2)}\}$$

$$\in \mathbf{R}^{L_1 \times L_2 \times (1+n)}, \quad (7)$$

where $n = n_1 + n_2$, \mathbf{S}_i denotes samples in the “same class”, and \mathbf{D}_i denotes samples in “different classes”. The representation in the dimensionality-reduced feature space of the patch is given by:

$$\text{Patch}(\mathbf{X}_i^*) = \{\mathbf{X}_i^*, \mathbf{S}_{i(1)}^*, \dots, \mathbf{S}_{i(n_1)}^*, \mathbf{D}_{i(1)}^*, \dots, \mathbf{D}_{i(n_2)}^*\} \\ \in \mathbf{R}^{d_1 \times d_2 \times (1+n)}. \quad (8)$$

To maintain discriminative information between samples in low dimensional space, the distances between \mathbf{X}_i^* and \mathbf{S}_i^* are supposed to be as small as possible while the distances between \mathbf{X}_i^* and \mathbf{D}_i^* are supposed to be as large as possible. Based on

this, the optimizations on the objective function are given below:

$$\arg \min_{\mathbf{X}_i^*} \sum_{j=1}^{n_1} D^2 \left(\mathbf{X}_i^* - \mathbf{S}_{i(j)}^* \right), \quad (9)$$

$$\arg \max_{\mathbf{X}_i^*} \sum_{j=1}^{n_2} D^2 \left(\mathbf{X}_i^* - \mathbf{D}_{i(j)}^* \right). \quad (10)$$

The two functions can be further simplified:

$$\arg \min_{\mathbf{X}_i^*} \sum_{j=1}^{n_1} D^2 \left(\mathbf{X}_i^* - \mathbf{S}_{i(j)}^* \right) - \alpha \sum_{j=1}^{n_2} D^2 \left(\mathbf{X}_i^* - \mathbf{D}_{i(j)}^* \right), \quad (11)$$

among which α is the weight coefficient. The weight vector is denoted as:

$$\beta = \left[\underbrace{1, \dots, 1}_{n_1}, \underbrace{-\alpha, \dots, -\alpha}_{n_2} \right]^T. \quad (12)$$

Then function (11) is simplified as

$$\begin{aligned} & \arg \min_{\mathbf{X}_i^*} \sum_{j=1}^{n_1} \beta_j D^2 \left(\mathbf{X}_i^* - \mathbf{S}_{i(j)}^* \right) \\ & + \sum_{j=1}^{n_2} \beta_{n_1+j} D^2 \left(\mathbf{X}_i^* - \mathbf{D}_{i(j)}^* \right) \\ & = \arg \min_{\mathbf{X}_i^*} \sum_{j=1}^n \beta_j \left\| \mathbf{X}_{P_i(1)}^* - \mathbf{X}_{P_i(1+j)}^* \right\|^2, \quad (13) \end{aligned}$$

where $\mathbf{X}_{P_i(1)}^*$ represents the first tensor sample in Patch(\mathbf{X}_i^*) and so on. Define the following matrix:

$$Q = \begin{bmatrix} \sum_{j=1}^n \beta_j & -\beta^T \\ -\beta & \text{diag}(\beta) \end{bmatrix} \in \mathbf{R}^{(1+n) \times (1+n)}. \quad (14)$$

Thus, the objective optimization function can be further represented as:

$$\arg \min_{\mathbf{X}_i^*} \sum_{g=1}^{n+1} \sum_{h=1}^{n+1} \left(Q_{g,h} \cdot \left[\mathbf{X}_{P_i(g)}^* \otimes \mathbf{X}_{P_i(h)}^*; (1:2)(1:2) \right] \right). \quad (15)$$

The whole objective optimization function of TDLA is obtained by summing over the patch optimization of each sample \mathbf{X}_i . However, different samples correspond to different local alignment Patch(\mathbf{X}_i), and thus it is not possible to add up the optimization objective functions of all samples directly. Hence, the local alignment of each sample needs to be unified into a full set of N training samples. The set of all samples is defined as:

$$\text{Whole}(\mathbf{X}) = \{\mathbf{X}_1, \dots, \mathbf{X}_N\} \in R^{L_1 \times L_2 \times N}. \quad (16)$$

Then each local alignment Patch(\mathbf{X}_i) is a subset of Whole(\mathbf{X}). The selection matrix $\mathbf{E}_i \in \mathbf{R}^{N \times (1+n)}$ is defined as:

$$\mathbf{E}_{i(a,b)} = \begin{cases} 1, & \text{if } a = F_i \{b\} \\ 0, & \text{else} \end{cases}, \quad (17)$$

among which $F_i \in \{i, i_1, \dots, i_n\}$ denotes the position of global indices of local samples in Patch(\mathbf{X}_i). Based on these points, the final representation of objective optimization function is derived by summing the patch optimizations of all samples, and it is denoted as:

$$\arg \min_{\mathbf{X}_1^*, \dots, \mathbf{X}_N^*} \sum_{g=1}^N \sum_{h=1}^N \left(\Omega_{g,h} \cdot \left[\mathbf{X}_g^* \otimes \mathbf{X}_h^*; (1:2)(1:2) \right] \right), \quad (18)$$

$$\Omega = \sum_{i=1}^N \mathbf{E}_i Q_i \mathbf{E}_i^T \in R^{N \times N}. \quad (19)$$

Putting (6) into (18) while bringing the constraints $\mathbf{U}_i^T \mathbf{U}_i = \mathbf{I}$, ($i = 1, 2$), the original object function is transferred into a new one for linear transformation matrix $\mathbf{U}_i \in \mathbf{R}^{L_i \times d_i}$, given by:

$$\arg \min_{\mathbf{U}_i^T \mathbf{U}_i = \mathbf{I}} \text{tr}(\mathbf{U}_i^T F(i) \mathbf{U}_i), \quad (20)$$

$$\begin{aligned} F(1) &= \sum_{g=1}^N \sum_{h=1}^N \Omega_{g,h} \cdot \text{Mat}_1 \left(\mathbf{X}_g \times_2 \mathbf{U}_2^T \right) \\ &\quad \cdot \text{Mat}_1^T \left(\mathbf{X}_h \times_2 \mathbf{U}_2^T \right), \quad (21) \end{aligned}$$

$$\begin{aligned} F(2) &= \sum_{g=1}^N \sum_{h=1}^N \Omega_{g,h} \cdot \text{Mat}_2 \left(\mathbf{X}_g \times_1 \mathbf{U}_1^T \right) \\ &\quad \cdot \text{Mat}_2^T \left(\mathbf{X}_h \times_1 \mathbf{U}_1^T \right). \quad (22) \end{aligned}$$

For given matrix $F(i)$, the solution of \mathbf{U}_i is the combination of eigen-vectors associated with the smallest d_i eigenvalues of $F(i)$. However, based on (21) and (22), $F(1)$ relies on \mathbf{U}_2 , and $F(2)$ relies on \mathbf{U}_1 . In this section, the optimal solution of transformation matrix \mathbf{U}_i is obtained by iterative optimization. Firstly, we initialize that $\mathbf{U}_i = \mathbf{I}_{d_i}$. Then $F(j)$, ($j = 1, 2; j \neq i$) is calculated depending on \mathbf{U}_i , and thus the next \mathbf{U}_j is obtained. Next, we execute iterations for $F(i)$. and \mathbf{U}_i based on the latest \mathbf{U}_j . The process is repeated until the iterations converge.

3.3. PolSAR Image Classification

The previous section described the method for solving the linear transformation matrices \mathbf{U}_1 and \mathbf{U}_2 based on training samples. $\mathbf{U}_1 \in \mathbf{R}^{L_1 \times d_1}$ can achieve feature compression of the original feature tensor in the polarimetric dimension, while $\mathbf{U}_2 \in \mathbf{R}^{L_2 \times d_2}$ achieves feature compression in the spatial dimension. According to Equation (6), the feature tensors of all pixels in the PolSAR image can be reduced to low-dimensional

feature vectors $\mathbf{X}^* \in \mathbf{R}^{d_1 \times d_2}$, which can extract the main features while maintaining good discriminative information between samples. Based on this, this paper uses the classic classifier SVM to obtain the final classification result. Figure 3 shows the flowchart of the proposed method for PolSAR image feature extraction and classification.

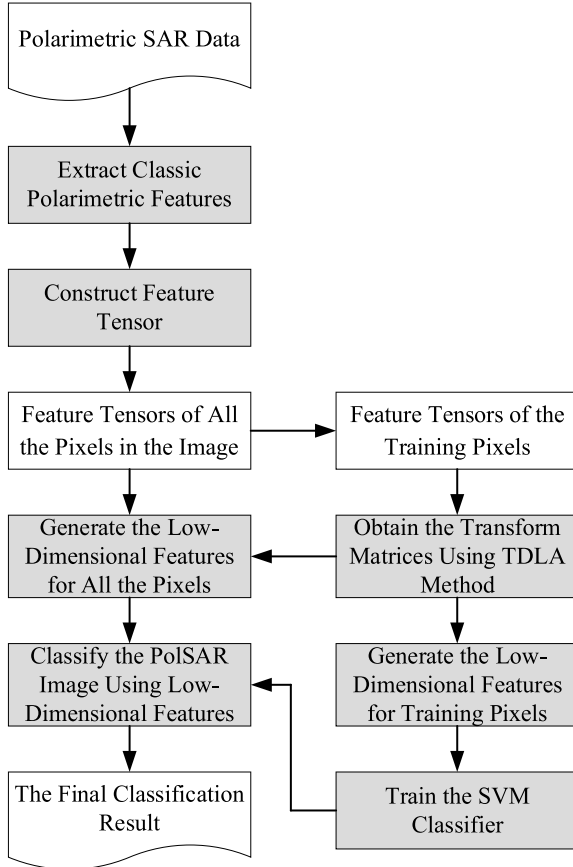


FIGURE 3. Flowchart of PolSAR feature extraction and classification.

4. EXPERIMENTAL RESULTS AND ANALYSIS

4.1. Introduction to Experimental Data

The experiment employed two sets of PolSAR data. The first data set is full polarimetric SAR data obtained by the Canadian Radarsat-2 system in the San Francisco area of the United States in 2009, with a image size of 1500×1400 pixels and a spatial resolution of 8 meters. Figure 4(a) shows the Pauli pseudo RGB image of the data, which includes different types of land covers, such as the ocean, vegetation, and buildings. In addition, buildings can be further divided into high-density urban areas, low-density urban areas, and inclined building areas. Since inclined buildings are easily confused with vegetation, this data is often used for the fine classification of ground objects and the research of scattering characteristics of buildings. Figure 4(b) shows the ground truth of the data.

The second set of data is full polarimetric SAR data obtained by the AIRSAR system in the EL Paso area of the United States, with a image size of 1000×1000 pixels and a spatial resolution of 4.6×3.3 meters. Figure 5(a) shows the Pauli pseudo

RGB image of the data, which includes different types of land covers, such as bare land, forests, parallel buildings (parallel to the radar flight direction), inclined buildings, and three types of crops. Figure 5(b) shows the ground truth of the data.

4.2. Parameter Setting and Analysis

There are several parameters to be set in the process of building feature tensors and finding solution of multilinear transformation matrices, where local alignment parameters n_1 , n_2 , and α are set with reference to the parameters in the original papers [27]. The experimental result shows that, through three iterations, TDLA algorithm converges at stable values and thus optimal solutions of transformation matrices \mathbf{U}_1 and \mathbf{U}_2 are obtained. Therefore, the maximum number of iterations is set to 10 to ensure convergence of TDLA algorithm. The remaining main parameters include the reduced feature dimensionalities d_1 and d_2 and the number of neighboring pixels, which will be analyzed in detail in the following experiments.

In the experiment, we first choose an 8-neighbor structure, so that the feature tensor of each pixel is denoted as $\mathbf{X} \in \mathbf{R}^{48 \times 9}$. For the reduced feature dimensionality d_i ($i = 1, 2$), based on the aforementioned analysis, the multilinear transformation matrix \mathbf{U}_i is determined by minimal d_i eigenvalues of $F(i)$. As a result, the setting of d_i is directly related to the distribution of the $F(i)$'s eigenvalues. The eigenvalues of $F(1)$ and $F(2)$ are sorted respectively in ascending order as shown in Figure 6. As seen from Figure 6(a), the eigenvalues corresponding to first order (which can also be referred to as the polarimetric feature dimension) are all negative, and the first three to five eigenvalues occupy the main component while the later ones gradually converge to zero. It is therefore reasonable to take a value of d_1 between three and five. To reduce the complexity of the subsequent classification, we set d_1 to 3. As illustrated in Figure 6(b), the eigenvalues corresponding to the second order (aka spatial dimension) are all negative as well, and the first eigenvalue takes up the main component which is extremely diverse from the later ones. So, the best value for d_2 is one. It is noted that the distribution of the eigenvalues is almost identical to that of Figure 5 when other neighbors are selected, so the setting of the feature dimensionalities d_1 and d_2 is not influenced by the structure of the neighbors.

When choosing different neighbors, the dimensions of low-dimension feature are the same, but the feature information contained is not, resulting in distinctions in classification. Based on different neighbor structures PolSAR classification experiments are carried out, and the corresponding Overall Accuracy (OA) is calculated. Figure 7 shows the variation curve of OA versus the number of neighbor pixels. It can be seen that OA grows rapidly as the number of neighbor pixels increases from 4 to 8 and remains almost constant when the number of neighbor pixels is 12 and 20. Therefore, the information of neighbor pixels contributes to the effectiveness of feature extraction and PolSAR classification. However, as the number of neighbor pixels further increases, OA gradually begins to fall. This is because larger neighbor structures may contain different kinds of land-cover pixels, thus affecting accurate extraction of the feature information in the central pixel. On the base of above

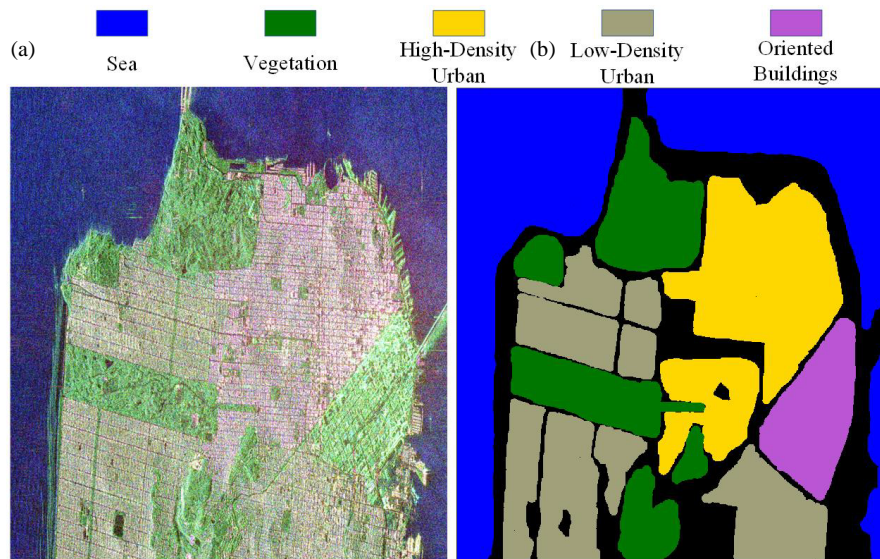


FIGURE 4. Polarimetric SAR data of San Francisco area. (a) Pauli pseudo RGB image; (b) Ground truth.

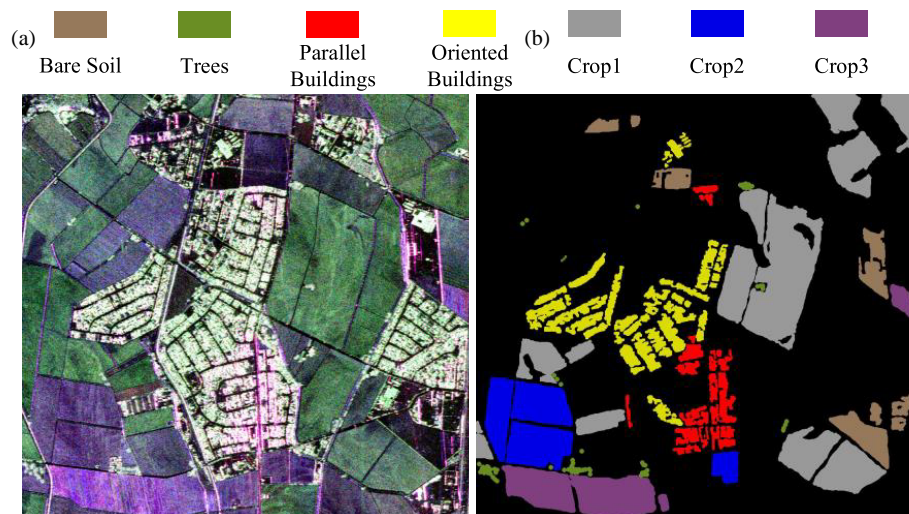


FIGURE 5. Polarimetric SAR data of EL Paso area. (a) Pauli pseudo RGB image; (b) Ground truth.

experimental results, 8-neighbor structure is utilized in this paper.

4.3. Comparison and Analysis of Classification Results

To verify the effectiveness of the proposed method, PCA, tSNE [36], and SGE [21], respectively representing traditional linear, nonlinear manifold learning, and supervised manifold learning dimensionality reduction method, were used for feature dimensionality reduction. Based on feature dimensionality reduction, classification experiments are conducted combined with the SVM method. In addition, the supervised Wishart classifier [3] is selected as the benchmark for classification performance evaluation. Figure 8 shows the variation curve of classification OA of different methods with feature dimensionalities. Overall, for the four feature dimensionality reduction methods, when the dimensionality of extracted feature is low, the infor-

mation contained in the feature is limited, which results in low classification accuracy. With the increase of feature dimensionality, the OA of these four methods exceeds that of Wishart classifier, gradually increasing to their maximum and stabilizing. The method in this paper can obtain the maximum accuracy when the feature dimensionality is greater than 3, which is consistent with the setting of parameter d_1 in the previous section. Compared with other methods, the proposed method can achieve the best classification accuracy at a low feature dimensionality, and the accuracy values have obvious advantages, indicating that the extracted features of the proposed method have better robustness and separability.

The classification results of different methods when achieving the best OA are shown in Figure 9, and the corresponding classification accuracy statistics are presented in Table 2. Figure 9(a) shows the result obtained by the Wishart classifier. It can be seen that, except for the ocean area, other ground ob-

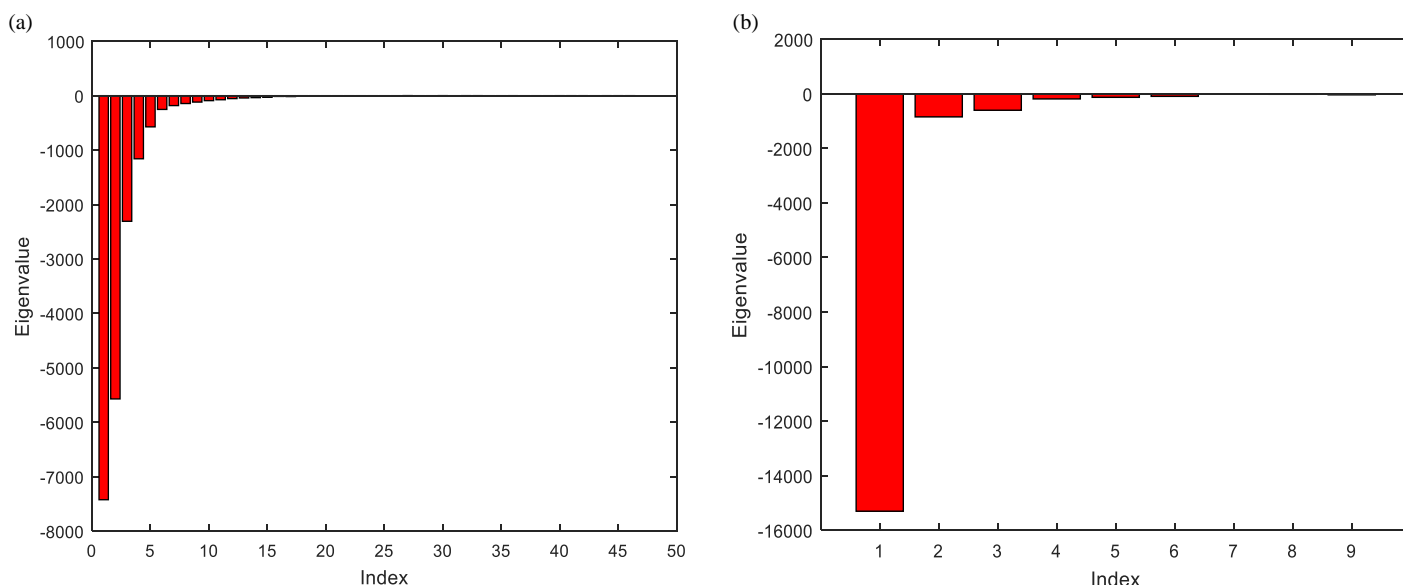


FIGURE 6. Eigenvectors in two dimensions. (a) First order; (b) Second order.

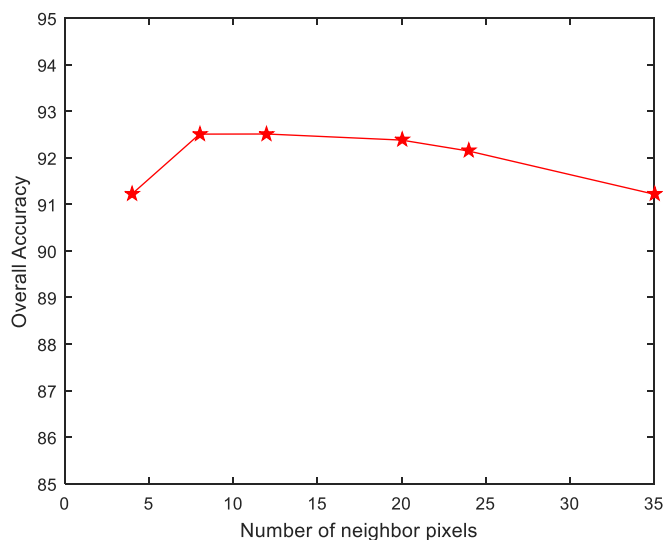


FIGURE 7. Classification accuracy versus the number of neighbor pixels.

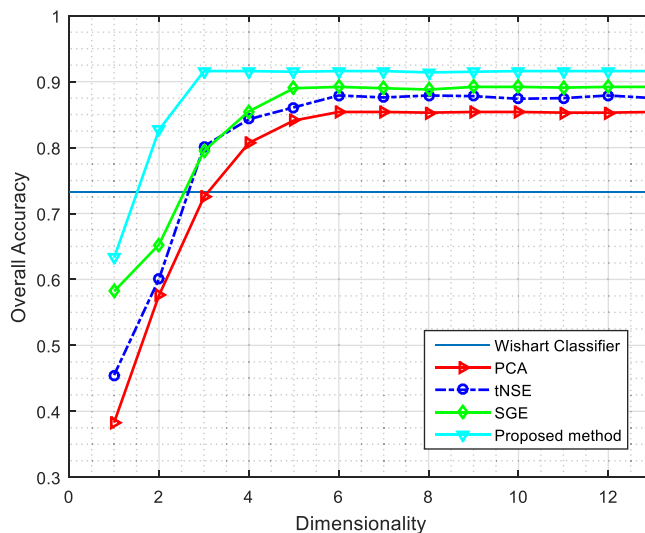


FIGURE 8. Classification OA and dimension curves of different methods.

TABLE 2. Classification accuracy of different methods on Radarsat-2 data.

Method	Wishart Classifier	PCA	tSNE	SGE	Proposed Method
Ocean	0.921	0.965	0.958	0.983	0.992
Vegetation	0.786	0.825	0.817	0.836	0.864
High-density urban areas	0.613	0.867	0.886	0.902	0.878
Low-density urban areas	0.555	0.763	0.809	0.817	0.913
Inclined building areas	0.627	0.735	0.890	0.814	0.896
Overall accuracy	0.732	0.854	0.879	0.892	0.916

ject types have serious misclassification, resulting in an overall classification accuracy of only 0.732. This is because this method only takes statistical probability into account and is

greatly affected by speckle noise. Figures 9(b)–(d) show the corresponding classification results of PCA, tSNE, and SGE, respectively. These methods perform dimensionality reduction

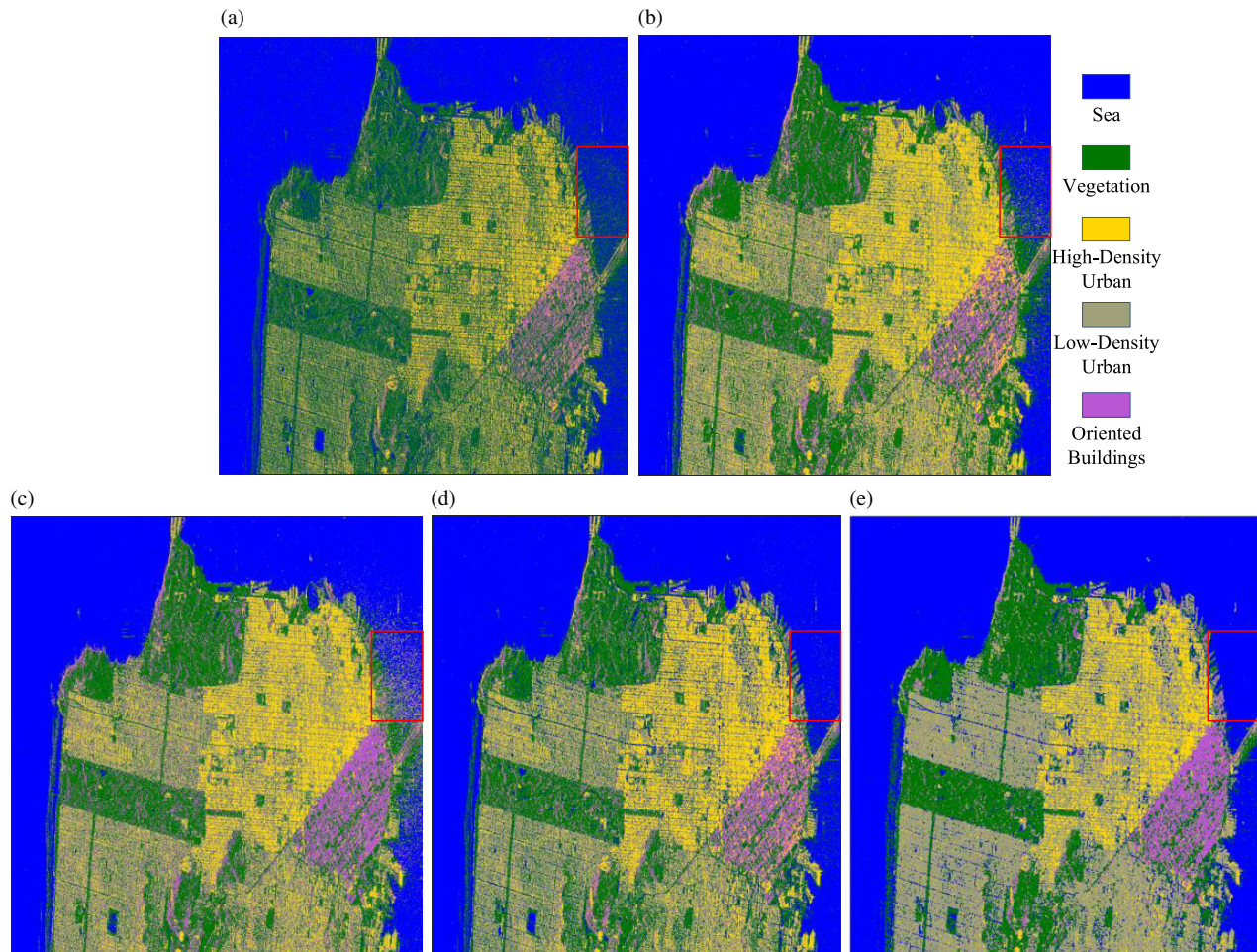


FIGURE 9. Classification results of different methods. (a) Wishart classifier; (b) PCA+SVM; (c) tNSE+SVM; (d) SGE+SVM; (e) The proposed method.

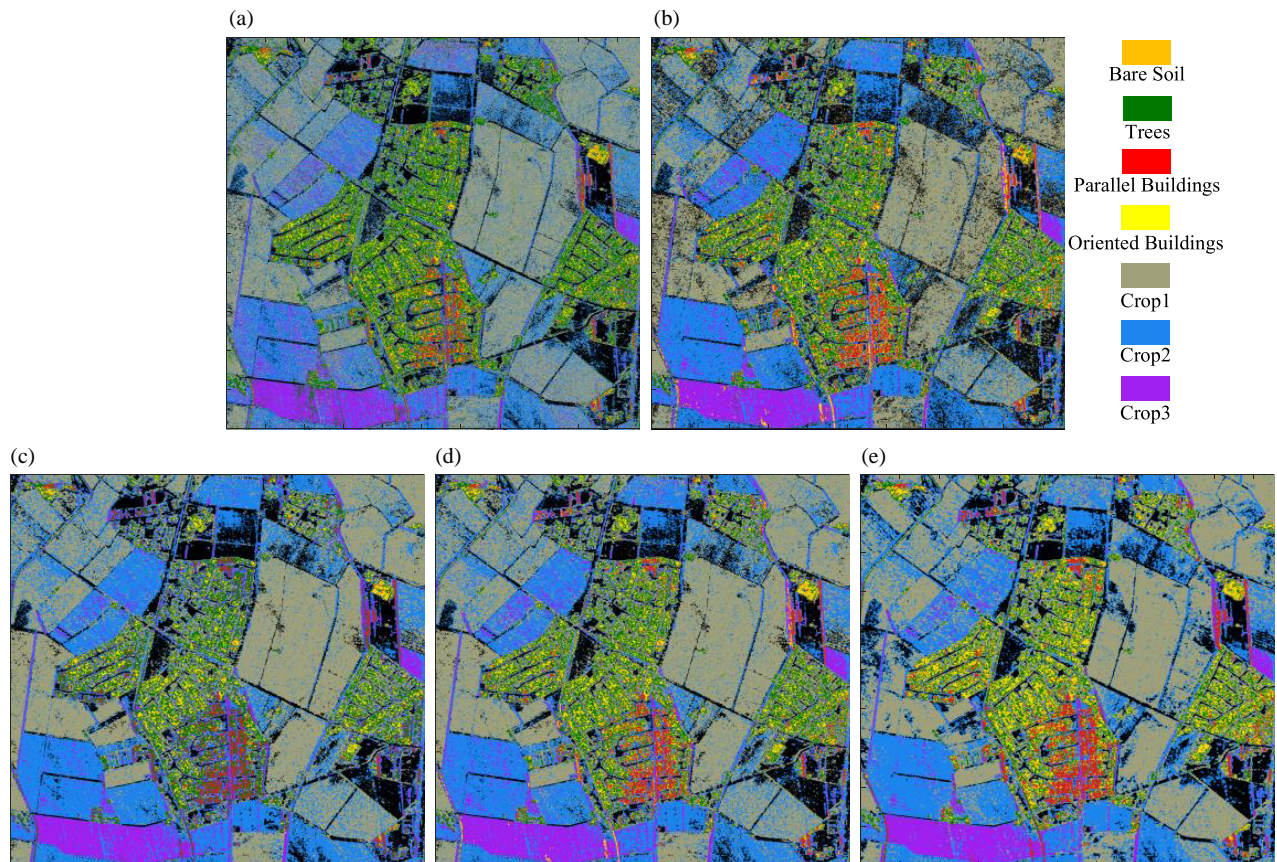
on the 48-dimensional feature vectors of each pixel, utilizing more information, resulting in significant improvement in overall classification accuracy compared to Figure 9(a). However, there are still some misclassifications in these result images. In Figure 9(b), a part of the inclined building areas is misclassified as high-density urban areas. PCA, as a linear dimensionality reduction method based on matrix algebra, cannot effectively remove the redundancy between features, making it difficult for the classifier to distinguish between samples of different classes. Its overall classification accuracy is 0.854. Figure 9(c) shows the result of tSNE method, with an overall classification accuracy of 0.879, which is better than the PCA method. Unlike the previous two methods, SGE method utilizes the class information of the samples during the feature dimensionality reduction process, so the obtained features have better separability, which further reduces the misclassification between different categories, as shown in Figure 9(d). The overall classification accuracy of SGE method is 0.892. Figure 9(e) shows the classification result of the proposed method, which has significantly improved classification performance with only a small number of misclassified points, resulting in an overall classification accuracy of 0.916. In addition, compared with other methods, the proposed method is less affected by speckle noise. This is be-

cause the proposed method uses a tensor composed of multiple feature vectors within the neighborhood to characterize each pixel, which can utilize the intrinsic spatial information of the image to suppress the influence of speckle noise and improve the robustness and accuracy of the extracted features. Taking the red rectangular area in the figure as an example, this area has a lot of noise, and it is difficult to see the spatial details near the coastline in Figures 9(a)–(d). In contrast, in Figure 9(e), the classification result for this area is very smooth, and the boundary and shape of the pier can be clearly seen. Therefore, the proposed method can effectively utilize both the polarimetric information and the spatial information of pixels, maintaining the spatial details of the image while achieving high-precision classification.

The classification results obtained by different methods on AIRSAR data are shown in Figure 10, and Table 3 presents the classification accuracy statistics, indicating that the proposed method achieves the best performance. It can be seen that the Wishart classifier results in a more severe misclassification and obvious noise, with an overall classification accuracy of only 0.706. In comparison, in the PCA method classification results shown in Figure 10(b), the classification effect of parallel buildings, crops 2, and crops 3 is improved, but there are still many

TABLE 3. Classification accuracy of different methods on AIRSAR data.

Method	Wishart Classifier	PCA	tSNE	SGE	Proposed Method
Bare soil	0.852	0.850	0.891	0.787	0.887
Trees	0.613	0.646	0.704	0.769	0.737
Parallel buildings	0.561	0.676	0.624	0.688	0.735
Oriented buildings	0.538	0.567	0.619	0.658	0.763
Crop 1	0.774	0.814	0.891	0.915	0.936
Crop 2	0.627	0.866	0.911	0.876	0.954
Crop 3	0.710	0.889	0.854	0.871	0.932
Overall accuracy	0.706	0.773	0.825	0.837	0.904

**FIGURE 10.** Classification results of different methods. (a) Wishart classifier; (b) PCA+SVM; (c) tSNE+SVM; (d) SGE+SVM; (e) The proposed method.

misclassifications, with a classification accuracy of 0.773. Figures 10(c) and 10(d) show the results based on the tSNE method and SGE method, respectively. The classification performance has been further improved because these two methods can better remove redundant parts among 48 features, and the extracted new features have better separability. The overall classification accuracies for these two methods are 0.825 and 0.837, respectively. Figure 10(e) shows the classification results of the proposed method, which significantly reduces misclassification compared to the previous methods, with an overall classification accuracy of 0.904. On the one hand, the proposed method

uses a tensor-based polarimetric-spatial feature representation form, which can effectively utilize the spatial information in the image to suppress the impact of speckle noise. On the other hand, this method utilizes the label information of samples in the dimensionality reduction process, and the separability of the extracted features can be well preserved. Therefore, the confusion phenomenon between some labels is significantly improved. In addition, it can be clearly seen from the figure that roads between different ground objects and within building areas are visible, indicating that the proposed method can maintain the spatial details of the image well.

In terms of calculating algorithm complexity, the computational load of the proposed method mainly focuses on solving linear transformation matrices, i.e., formulas (20)–(22). In each iteration, the computational complexity for solving U_1 is $O(N^2(2L_1L_2d_2 + L_1^2)) + O(L_1^3)$ and for solving U_2 is $O(N^2(2L_1L_2d_1 + L_2^2)) + O(L_2^3)$. Therefore, the computational complexity for m iterations is $O(mN^2(2L_1L_2d_2 + 2L_1L_2d_1 + L_1^2 + L_2^2)) + O(mL_1^3 + mL_2^3)$. For PCA, tSNE, and SGE methods, the computational complexity is $O(L_1^3)$. Therefore, the computational complexity of the proposed method is higher than that of traditional feature dimensionality reduction methods. Table 4 shows the computation time of these methods on different datasets. All experiments were run on a desktop computer using the MATLAB programming language. The computer's CPU was an Intel Core i7-7700 with a clock speed of 3.6 GHz and 16 GB of memory.

TABLE 4. Execution time comparison of different methods.

Method	PCA	tSNE	SGE	Proposed Method
Radarsat-2 data set	5.3 s	7.6 s	8.5 s	17.1 s
AIRSAR data set	3.7 s	5.4 s	6.3 s	13.4 s

5. CONCLUSIONS

The polarimetric target decomposition theory provides various features for analyzing target scattering characteristics and classifying PolSAR images. However, effectively utilizing these features to improve the classification accuracy of PolSAR images is still a challenging problem. This paper proposes a supervised manifold learning-based method for polarimetric feature extraction and classification. First, by combining multiple polarimetric feature vectors within the local neighborhood, use feature tensors to characterize the information of each pixel. This form helps to utilize the intrinsic spatial information in the image, thus suppressing the influence of speckle noise. Based on this, inspired by the local arrangement theory, use the TDLA method to seek a multilinear transformation matrix for dimensionality reduction. Since this method utilizes the label information of training samples, after dimensionality reduction, features can better preserve the separability between different labels. Classification experiments are carried out on Radarsat-2 data in the San Francisco area and AIRSAR data in the EL Paso area. The results show that proposed method achieves higher classification accuracy than traditional methods while effectively preserving spatial details in the image.

ACKNOWLEDGEMENT

This work was supported by the Science and Technology Innovation Program of Hunan Province (No. 2023RC3019), China Postdoctoral Science Foundation (No. 2020TQ0082), the Scientific Research Program of Hunan Provincial Department of Education (No. 22B0258), and Natural Science Foundation of Hunan Province (No. 2024JJ5649).

REFERENCES

- [1] Wang, X. and S. Chen, "Polarimetric synthetic aperture radar interpretation and recognition: Advances and perspectives," *Journal of Radars*, Vol. 9, No. 2, 259–276, 2020.
- [2] Dong, H., L. Si, W. Qiang, W. Miao, C. Zheng, Y. Wu, and L. Zhang, "A polarimetric scattering characteristics-guided adversarial learning approach for unsupervised PolSAR image classification," *Remote Sensing*, Vol. 15, No. 7, 1782, 2023.
- [3] Lee, J.-S., M. R. Grunes, and R. Kwok, "Classification of multi-look polarimetric SAR imagery based on complex Wishart distribution," *International Journal of Remote Sensing*, Vol. 15, No. 11, 2299–2311, 1994.
- [4] Formont, P., F. Pascal, G. Vasile, J.-P. Ovarlez, and L. Ferro-Famil, "Statistical classification for heterogeneous polarimetric SAR images," *IEEE Journal of Selected Topics in Signal Processing*, Vol. 5, No. 3, 567–576, 2011.
- [5] Cloude, S. R. and E. Pottier, "An entropy based classification scheme for land applications of polarimetric SAR," *IEEE Transactions on Geoscience and Remote Sensing*, Vol. 35, No. 1, 68–78, 1997.
- [6] Gou, S., X. Qiao, X. Zhang, W. Wang, and F. Du, "Eigenvalue analysis-based approach for POL-SAR image classification," *IEEE Transactions on Geoscience and Remote Sensing*, Vol. 52, No. 2, 805–818, 2014.
- [7] Lee, J.-S., M. R. Grunes, E. Pottier, and L. Ferro-Famil, "Unsupervised terrain classification preserving polarimetric scattering characteristics," *IEEE Transactions on Geoscience and Remote Sensing*, Vol. 42, No. 4, 722–731, 2004.
- [8] Wang, W., D. Xiang, J. Zhang, and J. Wan, "Integrating contextual information with H/α decomposition for PolSAR data classification," *IEEE Geoscience and Remote Sensing Letters*, Vol. 13, No. 12, 2034–2038, 2016.
- [9] Zhang, L., S. Zhang, H. Dong, and S. Zhu, "Robust classification of PolSAR images based on pinball loss support vector machine," *Journal of Radars*, Vol. 8, No. 4, 448–457, 2019.
- [10] Freeman, A. and S. L. Durden, "A three-component scattering model for polarimetric SAR data," *IEEE Transactions on Geoscience and Remote Sensing*, Vol. 36, No. 3, 963–973, 1998.
- [11] Yamaguchi, Y., T. Moriyama, M. Ishido, and H. Yamada, "Four-component scattering model for polarimetric SAR image decomposition," *IEEE Transactions on Geoscience and Remote Sensing*, Vol. 43, No. 8, 1699–1706, 2005.
- [12] Zhang, L., B. Zou, H. Cai, and Y. Zhang, "Multiple-component scattering model for polarimetric SAR image decomposition," *IEEE Geoscience and Remote Sensing Letters*, Vol. 5, No. 4, 603–607, 2008.
- [13] Xiang, D., Y. Ban, and Y. Su, "Model-based decomposition with cross scattering for polarimetric SAR urban areas," *IEEE Geoscience and Remote Sensing Letters*, Vol. 12, No. 12, 2496–2500, 2015.
- [14] Quan, S., B. Xiong, D. Xiang, and G. Kuang, "Derivation of the orientation parameters in built-up areas: With application to model-based decomposition," *IEEE Transactions on Geoscience and Remote Sensing*, Vol. 56, No. 8, 4714–4730, 2018.
- [15] Huang, X. and X. Nie, "Multi-view feature selection for PolSAR image classification via $l_{2,1}$ sparsity regularization and manifold regularization," *IEEE Transactions on Image Processing*, Vol. 30, 8607–8618, 2021.
- [16] Licciardi, G., R. G. Avezano, F. D. Frate, G. Schiavon, and J. Chanussot, "A novel approach to polarimetric SAR data processing based on nonlinear PCA," *Pattern Recognition*, Vol. 47, No. 5, 1953–1967, 2014.

- [17] Tu, S. T., J. Y. Chen, W. Yang, and H. Sun, "Laplacian eigenmaps-based polarimetric dimensionality reduction for SAR image classification," *IEEE Transactions on Geoscience and Remote Sensing*, Vol. 50, No. 1, 170–179, 2011.
- [18] Ainsworth, T. L. and J. S. Lee, "Optimal polarimetric decomposition variables-non-linear dimensionality reduction," in *IGARSS 2001, Scanning the Present and Resolving the Future. Proceedings. IEEE 2001 International Geoscience and Remote Sensing Symposium (Cat. No.01CH37217)*, Vol. 2, 928–930, 2001.
- [19] Ainsworth, T. L. and J.-S. Lee, "Polarimetric SAR image classification-exploiting optimal variables derived from multiple-image datasets," in *IGARSS 2004, 2004 IEEE International Geoscience and Remote Sensing Symposium*, Vol. 1, 2004.
- [20] Huang, X., X. Nie, and H. Qiao, "PolSAR image feature extraction via co-regularized graph embedding," *Remote Sensing*, Vol. 12, No. 11, 1738, 2020.
- [21] Shi, L., L. Zhang, J. Yang, L. Zhang, and P. Li, "Supervised graph embedding for polarimetric SAR image classification," *IEEE Geoscience and Remote Sensing Letters*, Vol. 10, No. 2, 216–220, 2013.
- [22] Lu, H., K. N. Plataniotis, and A. N. Venetsanopoulos, "A survey of multilinear subspace learning for tensor data," *Pattern Recognition*, Vol. 44, No. 7, 1540–1551, 2011.
- [23] Deng, Y.-J., H.-C. Li, K. Fu, Q. Du, and W. J. Emery, "Tensor low-rank discriminant embedding for hyperspectral image dimensionality reduction," *IEEE Transactions on Geoscience and Remote Sensing*, Vol. 56, No. 12, 7183–7194, 2018.
- [24] Wang, Q. and Y. Gu, "A discriminative tensor representation model for feature extraction and classification of multispectral LiDAR data," *IEEE Transactions on Geoscience and Remote Sensing*, Vol. 58, No. 3, 1568–1586, 2020.
- [25] Xu, D., S. Yan, L. Zhang, S. Lin, H.-J. Zhang, and T. S. Huang, "Reconstruction and recognition of tensor-based objects with concurrent subspaces analysis," *IEEE Transactions on Circuits and Systems for Video Technology*, Vol. 18, No. 1, 36–47, 2008.
- [26] Renard, N. and S. Bourennane, "Dimensionality reduction based on tensor modeling for classification methods," *IEEE Transactions on Geoscience and Remote Sensing*, Vol. 47, No. 4, 1123–1131, 2009.
- [27] Zhang, L., L. Zhang, D. Tao, and X. Huang, "Tensor discriminative locality alignment for hyperspectral image spectral-spatial feature extraction," *IEEE Transactions on Geoscience and Remote Sensing*, Vol. 51, No. 1, 242–256, 2013.
- [28] Tao, M., F. Zhou, Y. Liu, and Z. Zhang, "Tensorial independent component analysis-based feature extraction for polarimetric SAR data classification," *IEEE Transactions on Geoscience and Remote Sensing*, Vol. 53, No. 5, 2481–2495, 2015.
- [29] Huang, X., H. Qiao, B. Zhang, and X. Nie, "Supervised polarimetric SAR image classification using tensor local discriminant embedding," *IEEE Transactions on Image Processing*, Vol. 27, No. 6, 2966–2979, 2018.
- [30] Kolda, T. G. and B. W. Bader, "Tensor decompositions and applications," *SIAM Review*, Vol. 51, No. 3, 455–500, 2009.
- [31] Cloude, S. R., "Target decomposition theorems in radar scattering," *Electronics Letters*, Vol. 21, 22–24, 1985.
- [32] Van Zyl, J. J., "Unsupervised classification of scattering behavior using radar polarimetry data," *IEEE Transactions on Geoscience and Remote Sensing*, Vol. 27, No. 1, 36–45, 1989.
- [33] Krogager, E., "New decomposition of the radar target scattering matrix," *Electronics Letters*, Vol. 18, No. 26, 1525–1527, 1990.
- [34] Huynen, J. R., "Phenomenological theory of radar target," Ph.D. dissertation, Technology University Delft, 1970.
- [35] An, W., C. Xie, X. Yuan, Y. Cui, and J. Yang, "Four-component decomposition of polarimetric SAR images with deorientation," *IEEE Geoscience and Remote Sensing Letters*, Vol. 8, No. 6, 1090–1094, 2011.
- [36] Maaten, Van der L. and G. Hinton, "Visualizing data using t-SNE," *Journal of Machine Learning Research*, Vol. 9, No. 11, 2579–2605, 2008.